Fourth-Order Accurate Three-Dimensional Compressible Boundary-Layer Calculations

Venkit Iyer*
Vigyan Research Associates, Hampton, Virginia
and
Julius E. Harris†
NASA Langley Research Center, Hampton, Virginia

A fourth-order accurate finite-difference procedure for solving compressible three-dimensional boundary-layer equations is presented and applied to wing and ellipsoid flows. The method is fourth-order accurate normal to the surface and second-order accurate in the streamwise and crossflow directions for arbitrary mesh increments. The procedure is validated for a number of standard test cases over a range of Mach numbers. An interface procedure is used to solve the surface Euler equations with the inviscid flow pressure field as the input to assure consistency at the boundary-layer edge. The importance of the interface procedure in ensuring accuracy in edge boundary conditions is discussed. Details of applying the method to solve laminar flow past wing- and fuselage-type bodies are presented.

Nomenclature

$\tilde{A}_i, B_i, C_i, D_i$ = coefficients in the transformed equations
a_i, b_i, c_i = ξ, η, ζ differencing parameters
C_f = skin friction coefficient based on freestream conditions
C_{ij} = metric coefficient terms
F = u/u_e
G = v/v_r
g_{12} = metric coefficient
H = total enthalpy
h_1, h_2 = metric coefficients in x, y directions
I = $\partial H/\partial\zeta$, normal derivative of H
i, j, k = indices in ξ, η, ζ directions
L = $\partial F/\partial\zeta$, normal derivative of F
$\bar{l}$ = $(\rho\mu)/(\rho_e\mu_e)$
$\bar{l}_3$ = $\bar{l}/\sigma$
M = $\partial G/\partial\zeta$, normal derivative of G
p = pressure
Q = solution vector
q = total velocity = $\sqrt{u^2 + v^2 + 2uv\, g_{12}/(h_1h_2)}$
Re_{ref} = reference Reynolds number, $(u^*_{\text{ref}}L^*\rho^*_{\text{ref}})/\mu^*_{\text{ref}}$
S_1 = surface length in ξ direction, $\int_0^\xi h_1\, d\xi$
T = temperature
t^* = boundary-layer thickness, z^* at $F = 0.99$
u, v, w = streamwise, crossflow, and boundary normal velocities
$\tilde{w}$ = stretched normal velocity, $w\sqrt{Re_{\text{ref}}}$
x, y, z = streamwise, crosswise, and boundary normal coordinates
$\tilde{z}$ = stretched normal coordinate, $z\sqrt{Re_{\text{ref}}}$
α = angle of attack
α_c = angle between surface tangent and chord
θ = T/T_e
Λ = sweep angle
μ = viscosity
ξ, η, ζ = transformed boundary-layer coordinates in x, y, z directions
ρ = density
σ = Prandtl number
ϕ = $\sqrt{\rho_e\mu_eS_1u_e}$

Reference Quantities

H^*_{ref} = reference total enthalpy, $(U^{*2}_\infty)/[(\gamma - 1)M^2_\infty]$
L^* = reference length
p^*_{ref} = reference pressure, $\rho_\infty U^{*2}_\infty$
T^*_{ref} = reference temperature, U^{*2}_∞/R^*
u^*_{ref} = reference velocity, U^*_∞
μ^*_r = reference viscosity, $\mu^*_r(T^*_{\text{ref}})$
ρ^*_{ref} = reference density, ρ^*_∞

Superscripts

$*$ = dimensional quantity

Subscripts

e = edge of boundary layer
∞ = freestream quantity
r, ref = reference quantity
w = wall value
1, 2 = x, y directions

Introduction

NAVIER-STOKES solutions for many complex aerodynamic shapes are now routinely obtained for relatively coarse grid-point distributions; however, the accuracy requirements for three-dimensional stability and transition prediction procedure require much finer grid-point distributions. Consequently, accurate and efficient solution procedures for the three-dimensional compressible boundary-layer equations are required. In addition to accuracy considerations for stability and transition prediction procedures, boundary-layer solutions can often be obtained in embedded regions at a fraction of the cost associated with obtaining Navier-Stokes solutions.

Numerical procedures and related software for two-dimensional boundary-layer flows are routinely used in design and analysis. An example of a widely used method is presented in Ref. 1 (see Ref. 2 for a tabular summary of related procedures). The theory and numerical algorithms used in these two-dimensional procedures cannot be extended directly to

Presented as Paper 89-0130 at the AIAA 27th Aerospace Sciences Meeting, Reno, NV, Jan. 9-12, 1989; received April 15, 1989; revision received July 19, 1989.

*Research Engineer. Member AIAA.
†Senior Research Scientist, Computational Methods Branch. Associate Fellow AIAA.

general three-dimensional flows due to the mixed parabolic-hyperbolic character of the three-dimensional equations (see Wang[3]). In addition to the problems associated with the mixed character of the equations, two initial data planes must be specified in order to numerically solve the system. In the present paper, a fourth-order numerical procedure for the three-dimensional compressible boundary-layer equations is presented and applied to flows past wing- and fuselage-type bodies.

Governing Equations

The three-dimensional boundary-layer equations in non-orthogonal surface coordinates are as follows (nondimensional):

$$\frac{\partial}{\partial x}(C_{11}\rho u) + \frac{\partial}{\partial y}(C_{12}\rho v) + C_{13}\frac{\partial}{\partial \tilde{z}}(\rho \tilde{w}) = 0 \tag{1}$$

$$\frac{u}{h_1}\frac{\partial u}{\partial x} + \frac{v}{h_2}\frac{\partial u}{\partial y} + \tilde{w}\frac{\partial u}{\partial \tilde{z}} + C_{24}u^2 + C_{25}uv + C_{26}v^2 = \frac{1}{\rho}\left[C_{27}\frac{\partial p}{\partial x} + C_{28}\frac{\partial p}{\partial y} + \frac{\partial}{\partial \tilde{z}}\left(\mu\frac{\partial u}{\partial \tilde{z}}\right)\right] \tag{2}$$

$$\frac{u}{h_1}\frac{\partial v}{\partial x} + \frac{v}{h_2}\frac{\partial v}{\partial y} + \tilde{w}\frac{\partial v}{\partial \tilde{z}} + C_{34}u^2 + C_{35}uv + C_{36}v^2 = \frac{1}{\rho}\left[C_{37}\frac{\partial p}{\partial x} + C_{38}\frac{\partial p}{\partial y} + \frac{\partial}{\partial \tilde{z}}\left(\mu\frac{\partial v}{\partial \tilde{z}}\right)\right] \tag{3}$$

$$\frac{u}{h_1}\frac{\partial H}{\partial x} + \frac{v}{h_2}\frac{\partial H}{\partial y} + \tilde{w}\frac{\partial H}{\partial \tilde{z}} = \frac{1}{\rho}\frac{\partial}{\partial \tilde{z}}\left[\frac{\mu}{\rho}\frac{\partial H}{\partial \tilde{z}} - \frac{u_{\text{ref}}^{*2}}{H_{\text{ref}}^{*}}\mu\left(\frac{1-\sigma}{\sigma}\right)\frac{\partial}{\partial \tilde{z}}\left(\frac{q^2}{2}\right)\right] \tag{4}$$

The coordinates x and y can be either orthogonal or non-orthogonal and lie on the body surface; the coordinate z is orthogonal to both x and y (surface-oriented monoclinic system; see Ref. 4). The metric tensor elements h_1, h_2, and g_{12} are obtained from the definition of the body surface and its partial derivatives. These quantities are defined in the reference frame Cartesian coordinates (x', y', z') as

$$h_1^2 = x_x'^2 + y_x'^2 + z_x'^2; \quad h_2^2 = x_y'^2 + y_y'^2 + z_y'^2$$
$$g_{12} = x_x'x_y' + y_x'y_y' + z_x'z_y' \tag{5}$$

The remaining terms are defined as follows:

$$C_{11} = \frac{\sqrt{g}}{h_1}; \quad C_{12} = \frac{\sqrt{g}}{h_2}; \quad C_{13} = \sqrt{g}; \quad g = h_1^2h_2^2 - g_{12}^2$$
$$C_{24} = \frac{g_{12}}{g}\left(\frac{g_{12}}{h_1^2}\frac{\partial h_1}{\partial x} + \frac{\partial h_1}{\partial y} - \frac{1}{h_1}\frac{\partial g_{12}}{\partial x}\right)$$
$$C_{25} = \frac{1}{g}\left\{h_1h_2\left[1 + \left(\frac{g_{12}}{h_1h_2}\right)^2\right]\frac{\partial h_1}{\partial y} - 2g_{12}\frac{\partial h_2}{\partial x}\right\}$$
$$C_{26} = \frac{h_1}{g}\left(\frac{\partial g_{12}}{\partial y} - h_2\frac{\partial h_2}{\partial x} - \frac{g_{12}}{h_2}\frac{\partial h_2}{\partial y}\right); \quad C_{27} = \frac{h_1h_2^2}{g}$$
$$C_{28} = \frac{h_1g_{12}}{g}; \quad C_{34} = \frac{h_2}{g}\left(\frac{\partial g_{12}}{\partial x} - h_1\frac{\partial h_1}{\partial y} - \frac{g_{12}}{h_1}\frac{\partial h_1}{\partial x}\right)$$
$$C_{35} = \frac{1}{g}\left\{h_1h_2\left[1 + \left(\frac{g_{12}}{h_1h_2}\right)^2\right]\frac{\partial h_2}{\partial x} - 2g_{12}\frac{\partial h_1}{\partial y}\right\}$$
$$C_{36} = \frac{g_{12}}{g}\left(\frac{g_{12}}{h_2^2}\frac{\partial h_2}{\partial y} + \frac{\partial h_2}{\partial x} - \frac{1}{h_2}\frac{\partial g_{12}}{\partial y}\right)$$
$$C_{37} = \frac{h_2g_{12}}{g}; \quad C_{38} = -\frac{h_1^2h_2}{g} \tag{6}$$

The surface Euler equations[5] are defined at the boundary-layer edge as $\tilde{z} \to \infty$

$$\frac{u_e}{h_1}\frac{\partial u_e}{\partial x} + \frac{v_e}{h_2}\frac{\partial u_e}{\partial y} + C_{24}u_e^2 + C_{25}u_ev_e + C_{26}v_e^2 = \frac{1}{\rho_e}\left(C_{27}\frac{\partial p}{\partial x} + C_{28}\frac{\partial p}{\partial y}\right) \tag{7}$$

$$\frac{u_e}{h_1}\frac{\partial v_e}{\partial x} + \frac{v_e}{h_2}\frac{\partial v_e}{\partial y} + C_{34}u_e^2 + C_{35}u_ev_e + C_{36}v_e^2 = \frac{1}{\rho_e}\left(C_{37}\frac{\partial p}{\partial x} + C_{38}\frac{\partial p}{\partial y}\right) \tag{8}$$

Given $p(x, y)$ and initial conditions, the foregoing equations can be solved for u_e and v_e for each downstream (x, y). This method is superior to interpolating the velocity components from the inviscid grid to the boundary-layer grid. Since the edge conditions are derived from a subset of the full three-dimensional boundary-layer equations, consistency and compatibility are assured. The correct behavior of the velocity components at the boundaries can also be enforced.[6]

Transformation of the Equations

The equations are transformed to the (ξ, η, ζ) plane in order to remove the singularity at $x = 0$ and reduce the growth of the boundary layer in the computational plane. The transformation variables are $\xi = x$, $\eta = y$ (these symbols will be used interchangeably; partial derivatives are distinct; $(\partial/\partial\xi)|_{\eta,\zeta}$ as against $(\partial/\partial x)|_{y,\tilde{z}}$, for example). A transformed normal coordinate ζ is defined as

$$\zeta = \frac{\phi(x, y)}{\rho_e\mu_eS_1}\int_0^{\tilde{z}}\rho\, d\tilde{z} \tag{9}$$

A new flow variable F is also defined as the ratio of u to the local edge value. The crossflow velocity is not scaled with respect to the edge value, since crossflow reversal at the boundary-layer edge may occur. Hence, G is defined as equal to v/u_e or v.

A new transformation normal velocity w is introduced such that

$$w = \tilde{w}\frac{S_1}{u_e}\frac{\partial \zeta}{\partial \tilde{z}} + \frac{S_1}{h_1}F\frac{\partial \zeta}{\partial x} + \frac{S_1}{h_2}G\frac{\partial \zeta}{\partial y} \tag{10}$$

The transformed momentum equations and energy equation are as follows:

$$\frac{\partial w}{\partial \zeta} = \tilde{A}_1\frac{\partial F}{\partial \xi} + \tilde{A}_2F + \tilde{A}_3\frac{\partial G}{\partial \eta} + \tilde{A}_4G \tag{11}$$

$$\frac{\partial}{\partial \zeta}(\bar{l}L - wF) = B_1\frac{\partial F^2}{\partial \xi} + B_2\frac{\partial FG}{\partial \eta} + B_3F^2 + B_4FG + B_5G^2 + B_6\theta \tag{12}$$

$$\frac{\partial}{\partial \zeta}(\bar{l}M - wG) = C_1\frac{\partial FG}{\partial \xi} + C_2\frac{\partial G^2}{\partial \eta} + C_3F^2 + C_4FG + C_5G^2 + C_6\theta \tag{13}$$

$$\frac{\partial}{\partial \zeta}(\bar{l}_3I - wH) = D_1\frac{\partial FH}{\partial \xi} + D_2\frac{\partial GH}{\partial \eta} + D_3FH + D_4GH + D_5 \tag{14}$$

The coefficients $\tilde{A}_i$, B_i, C_i, D_i are functions of the edge conditions (except for D_5, the viscous dissipation term). These coefficients and associated parameters are defined in the Appendix. The equations can be simplified for a number of

limiting cases at the flow boundaries. These are the line of symmetry equations, the infinite swept-wing equations, similarity flow equations, the attachment line equations, and the stagnation point equations. Equation (3) is singular for symmetry line flow; consequently, it is differentiated with respect to y and transformed using Eq. (9). For attachment line flow, the x momentum equation [Eq. (2)] becomes singular at $x = 0$. Differentiation with respect to x and a transformation similar to Eq. (9) yields the attachment line equation. These equations are in quasi-two-dimensional form and can be solved independent of the three-dimensional region.

Discretization of the Equations

The discretization procedure for the momentum equations is as follows:

$$\boldsymbol{Q} \equiv \begin{bmatrix} \bar{l}\dfrac{\partial F}{\partial \zeta} - wF \\ \bar{l}\dfrac{\partial G}{\partial \zeta} - wG \\ F \\ G \end{bmatrix} = \begin{bmatrix} \bar{l}L - wF \\ \bar{l}M - wG \\ F \\ G \end{bmatrix} \tag{15}$$

$\boldsymbol{Q}'$ can be obtained from the transformed equations [Eqs. (12) and (13)] as

$$\boldsymbol{Q}' = \begin{bmatrix} B_1\dfrac{\partial F^2}{\partial \xi} + B_2\dfrac{\partial FG}{\partial \eta} + B_3F^2 + B_4FG + B_5G^2 + B_6\theta \\ C_1\dfrac{\partial FG}{\partial \xi} + C_2\dfrac{\partial G^2}{\partial \eta} + C_3F^2 + C_4FG + C_5G^2 + C_6\theta \\ L \\ M \end{bmatrix} \tag{16}$$

$\boldsymbol{Q}''$ can be obtained by differentiating Eq. (16) and using Eq. (11) as

$$\boldsymbol{Q}'' = \begin{bmatrix} 2B_1\dfrac{\partial}{\partial \xi}FL + B_2\dfrac{\partial}{\partial \eta}(FM + GL) + 2B_3FL + B_4(FM + GL) + 2B_5GM + B_6\theta' \\ C_1\dfrac{\partial}{\partial \xi}(FM + GL) + 2C_2\dfrac{\partial}{\partial \eta}GM + 2C_3FL + C_4(FM + GL) + 2C_5GM + C_6\theta' \\ \dfrac{1}{\bar{l}}\left[\dfrac{1}{2}B_1\dfrac{\partial}{\partial \xi}F^2 + B_2G\dfrac{\partial}{\partial \eta}F + \tilde{B}_3F^2 + \tilde{B}_4FG + B_5G^2 + B_6\theta + L(w - \bar{l}')\right] \\ \dfrac{1}{\bar{l}}\left[C_1F\dfrac{\partial}{\partial \xi}G + \dfrac{1}{2}C_2\dfrac{\partial}{\partial \eta}G^2 + C_3F^2 + \tilde{C}_4FG + \tilde{C}_5G^2 + B_6\theta + M(w - \bar{l}')\right] \end{bmatrix} \tag{17}$$

A finite-difference approximation accurate to the fourth order in ζ for arbitrary $\Delta\zeta$ is required. The two-point compact $O(\Delta\zeta)^4$ procedure allows the use of substantially less mesh points normal to the wall boundary than traditional $O(\Delta\zeta)^2$ procedures for a specified level of accuracy. The following equation can be written at $k - \frac{1}{2}$ (with $\Delta\zeta = \zeta_k - \zeta_{k-1}$):

$$\boldsymbol{Q}_k - \boldsymbol{Q}_{k-1} - \frac{\Delta\zeta}{2}\left(\boldsymbol{Q}'_k + \boldsymbol{Q}'_{k-1}\right) + \frac{\Delta\zeta^2}{12}\left(\boldsymbol{Q}''_k + \boldsymbol{Q}''_{k-1}\right) + O(\Delta\zeta)^5 = 0 \tag{18}$$

The resultant system is of (4×4) block tridiagonal form in F, G, L, and M. One major advantage of this scheme is the application of wall and edge conditions. For km points in ζ, the system yields $4 \cdot (km - 1)$ equations in $4 \cdot km$ unknowns. The additional four equations are the no-slip boundary conditions, $F_1 = G_1 = 0$, and the edge conditions, $F_{km} = 1$, $G_{km} = v_e$.

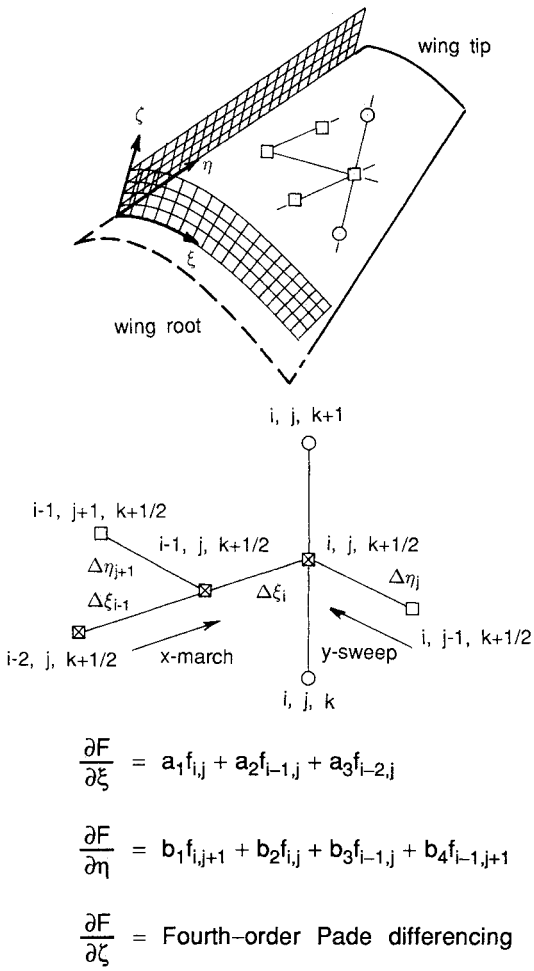

Fig. 1 Finite-difference molecule for three-dimensional boundary-layer solution.

The discretization in the stream surface directions (ξ, η) is $O(\Delta^2)$. The grid points involved in the finite-difference approximation at $(i, j, k + \frac{1}{2})$ are shown in Fig. 1. The $\partial/\partial\xi$ terms are replaced by a three-point backward formula and $\partial/\partial\eta$ terms by a four-point zig-zag scheme in order to correctly represent crossflow reversal. Nonlinear terms are linearized by Newton linearization. Iterative updates for δF, δG, δL, δM are calculated at each step for the linear system. Application of the ζ, ξ, and η differencing schemes and Newton linearization yields a system of equations at each midpoint $k + \frac{1}{2}$ as follows:

$$a_{k-1}S_{k-1} + b_kS_k = r_k$$

where

$$S_k = (\delta F_k, \delta G_k, \delta L_k, \delta M_k)^T \tag{19}$$

The 4×4 blocks of a, b and the 4×1 vector r are given in Table 1 of Ref. 7. At the wall, the boundary condition

$\delta F_1 = \delta G_1 = 0$ is applied. As a result, the discretized system is down-shifted by two rows, yielding a block-tridiagonal structure. The lower diagonal block α_k, the diagonal block β_k, the upper diagonal block γ_k, and the right-hand side vector δ_k are as follows:

$$\alpha_k = \begin{bmatrix} a_{11}^{k-1} & a_{12}^{k-1} & a_{13}^{k-1} & a_{12}^{k-1} \\ a_{21}^{k-1} & a_{22}^{k-1} & a_{23}^{k-1} & a_{24}^{k-1} \\ 0 & 0 & 0 & 0 \\ 0 & 0 & 0 & 0 \end{bmatrix}$$

$$\beta_k = \begin{bmatrix} b_{11}^{k-1} & b_{12}^{k-1} & b_{13}^{k-1} & b_{14}^{k-1} \\ b_{21}^{k-1} & b_{22}^{k-1} & b_{23}^{k-1} & b_{24}^{k-1} \\ a_{31}^{k} & a_{32}^{k} & a_{33}^{k} & a_{34}^{k} \\ a_{41}^{k} & a_{42}^{k} & a_{43}^{k} & a_{44}^{k} \end{bmatrix}$$

$$\gamma_k = \begin{bmatrix} 0 & 0 & 0 & 0 \\ 0 & 0 & 0 & 0 \\ b_{31}^{k+1} & b_{32}^{k+1} & b_{33}^{k+1} & b_{34}^{k+1} \\ b_{41}^{k+1} & b_{42}^{k+1} & b_{43}^{k+1} & b_{44}^{k+1} \end{bmatrix}, \quad \delta_k = \begin{bmatrix} r_1^{k-1} \\ r_2^{k-1} \\ r_3^{k} \\ r_4^{k} \end{bmatrix} \tag{20}$$

The resulting system is

$$\alpha_k S_{k-1} + \beta_k S_k + \gamma_{k+1} S_{k+1} = \delta_k \tag{21}$$

The boundary conditions at the wall and the boundary-layer edge modify the diagonal block and the RHS vector, resulting in

$$\beta_1 = \begin{bmatrix} 1 & 0 & 0 & 0 \\ 0 & 1 & 0 & 0 \\ a_{31}^{1} & a_{32}^{1} & a_{33}^{1} & a_{34}^{1} \\ a_{41}^{1} & a_{42}^{1} & a_{43}^{1} & a_{44}^{1} \end{bmatrix}, \quad \beta_{km} = \begin{bmatrix} b_{11}^{km} & b_{12}^{km} & b_{13}^{km} & b_{14}^{km} \\ b_{21}^{km} & b_{22}^{km} & b_{23}^{km} & b_{24}^{km} \\ 1 & 0 & 0 & 0 \\ 0 & 1 & 0 & 0 \end{bmatrix}$$

$$\delta_1 = [0 \quad 0 \quad r_3^1 \quad r_4^1]^T, \quad \delta_{km} = [r_1^{km} \quad r_2^{km} \quad 0 \quad 0]^T \tag{22}$$

For the solution of the energy equation, the system consists of 2×2 blocks. The $\boldsymbol{Q}$, $\boldsymbol{Q}'$, and $\boldsymbol{Q}''$ vectors are

$$\boldsymbol{Q} \equiv \begin{bmatrix} \bar{l}_3 I - wH \\ H \end{bmatrix} \tag{23}$$

$$\boldsymbol{Q}' = \begin{bmatrix} D_1 \dfrac{\partial FH}{\partial \xi} + D_2 \dfrac{\partial GH}{\partial \eta} + D_3 FH + D_4 GH + D_5 \\ I \end{bmatrix} \tag{24}$$

$$\boldsymbol{Q}'' = \begin{bmatrix} D_1 \dfrac{\partial}{\partial \xi}(FI + HL) + D_2 \dfrac{\partial}{\partial \eta}(GI + HM) + D_3(FI + HL) + D_4(GI + HM) + D_5' \\ \dfrac{1}{\bar{l}_3}\left[D_1 F \dfrac{\partial H}{\partial \xi} + D_2 G \dfrac{\partial H}{\partial \eta} + D_5 + I(w - \bar{l}_3') \right] \end{bmatrix} \tag{25}$$

The finite-difference scheme for the energy equation is identical to that used for the momentum equations, however, the block-tridiagonal system is set up to solve for H and I rather than δH and δI since this produces a more diagonally dominant system for solving the energy equation. The a_{ij}, b_{ij}, and r_i corresponding to the following system are given in Table 2 of Ref. 7.

$$a_{k-1} S_{k-1} + b_k S_k = r_k$$

where

$$S_k = (H_k, I_k)^T \tag{26}$$

For the adiabatic wall boundary condition, β_1 and δ_1 blocks at the wall become

$$\beta_1 = \begin{bmatrix} 0 & 1 \\ a_{21}^1 & a_{22}^1 \end{bmatrix}, \quad \delta_1 = \begin{bmatrix} 0 \\ r_2^1 \end{bmatrix} \tag{27}$$

If a heat flux or temperature distribution is specified, the corresponding β_1 and δ_1 are as follows:

$$\beta_1 = \begin{bmatrix} 1 & 0 \\ a_{21}^1 & a_{22}^1 \end{bmatrix}, \quad \delta_1 = \begin{bmatrix} H_w \\ r_2^1 \end{bmatrix} \tag{28}$$

The application of the fourth-order scheme to the integration of the continuity equation yields

$$w_k = w_{k-1} + \frac{\Delta\zeta}{2}(w'_k + w'_{k-1}) - \frac{\Delta\zeta^2}{12}(w''_k - w''_{k-1}) \tag{29}$$

where

$$w' = \tilde{A}_1 \frac{\partial F}{\partial \xi} + \tilde{A}_2 F + \tilde{A}_3 \frac{\partial G}{\partial \eta} + \tilde{A}_4 G$$

$$w'' = \tilde{A}_1 \frac{\partial L}{\partial \xi} + \tilde{A}_2 L + \tilde{A}_3 \frac{\partial M}{\partial \eta} + \tilde{A}_4 M \tag{30}$$

The integration proceeds with a specified value of w_1, the mass injection at the wall. The solution of the continuity equation is decoupled from the solution of the momentum and energy equations for simplicity. Convergence can be accelerated by coupling at the expense of inversion of a system with 5×5 tridiagonal blocks.

Interface Procedure

An interface program is used to process the input inviscid data and geometry. The individual features of the inviscid flow and geometry can be dealt with in the interface procedure. This permits the solution of the boundary layer to be performed relatively independent of the selected inviscid software and body geometry. As an example, the interfacing steps for wing flow are briefly discussed (see Refs. 6 and 7 for a more complete discussion). First, the inviscid attachment line is accurately located by an iterative grid interpolation procedure such that the velocity vector on this line is exactly tangential to it. Second, the boundary-layer surface grid is algebraically generated on the lower or upper surface to the required resolution, followed by calculation of the metrics. Next, the inviscid pressure field is interpolated from the coarse inviscid grid to the fine boundary-layer grid by smooth tension splines. Finally, the surface Euler equations [Eqs. (7) and (8)] are solved with appropriate initial and boundary conditions to obtain the edge velocities u_e and v_e consistent with the boundary-layer equations. Direct interpolation of the velocity vectors from a coarse inviscid grid to the fine boundary-layer grid can give rise to large errors, especially in the boundary-adjacent regions, where accuracy is critical.

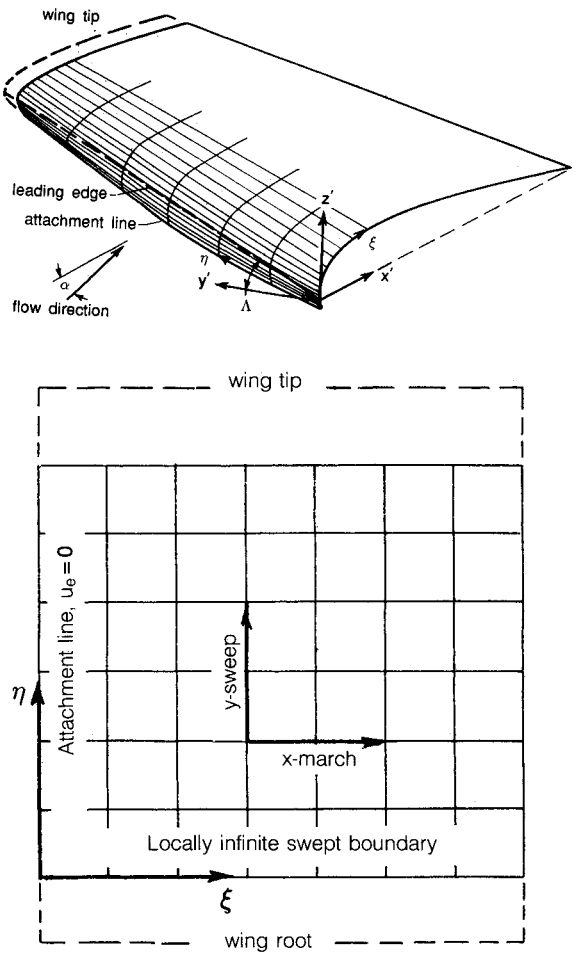

Fig. 2 Solution boundaries and marching directions.

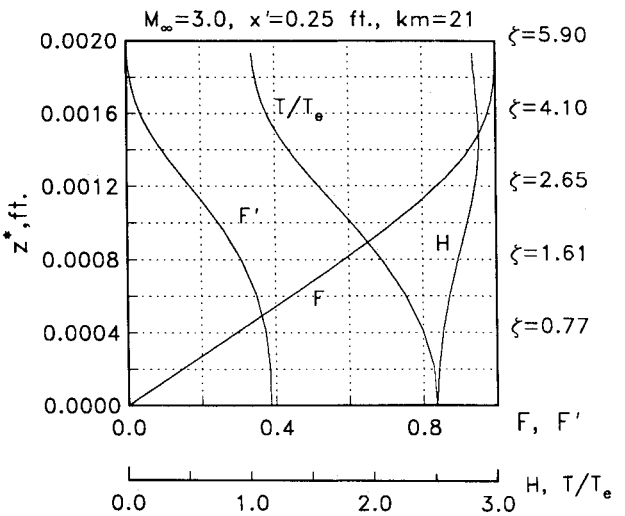

Fig. 3 Solution profiles for supersonic flow past flat plate.

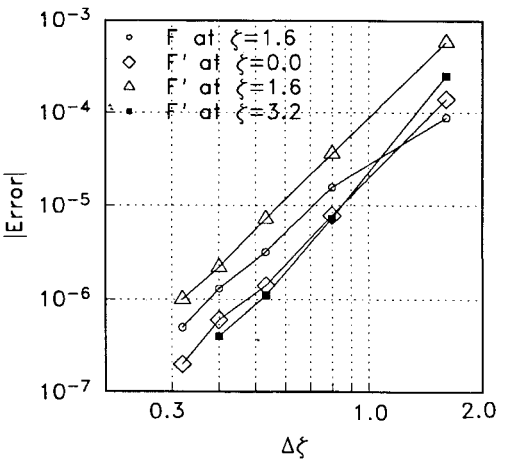

Fig. 4 Variation of solution accuracy with interval size.

Solution Procedure

The boundary-layer solution is initiated with a specified distribution of the x, y, h_1, h_2, u_e, and v_e values. At each station, the edge parameters that enter into the boundary-layer solution scheme originate from the metrics and the edge velocities. From h_1, h_2, g_{12} and their gradients $\partial h_1/\partial x$, $\partial h_1/\partial y$, $\partial h_2/\partial x$, $\partial h_2/\partial y$, $\partial g_{12}/\partial x$, $\partial g_{12}/\partial y$, the values of C_{13}, C_{24}, C_{25}, C_{26}, C_{34}, C_{35}, C_{36}, and S_1 are calculated. From u_e, v_e, $(\rho_e \mu_e)$ and gradients $\partial u_e/\partial \xi$, $\partial u_e/\partial \eta$, $\partial v_e/\partial \xi$, $\partial v_e/\partial \eta$, the values of ϕ, $\partial/\partial \xi$ $(C_{13}\phi/h_1)$ and $\partial/\partial \eta$ $(C_{13}\phi/h_2 u_e)$ are calculated. Finally, $\tilde{A}_1$, $\tilde{A}_2$, $\tilde{A}_3$, $\tilde{A}_4$, B_3, B_4, B_5, C_3, C_4, C_5 are the independent edge quantities obtained from all of the foregoing that enter into the boundary-layer solution routine. The temperature T is used in the update of the viscosity and density terms in $\bar{l}$, $\bar{l}'$, θ, and θ'. The parameter D_5 in the energy equation can be calculated once F, G, L, and M are known. As stated earlier, some of the terms in the transformed equations vanish for special cases of flow at boundaries. However, the basic momentum and energy equation solvers are designed for the general form of the equations with appropriate logic to handle the simplified cases.

The solution procedure for flow past a swept wing is chosen as an example problem. For a wing of arbitrary planform and taper, one suitable grid that can be used is the body-oriented nonorthogonal grid consisting of constant chord and constant span lines as shown in Fig. 2. The grid originates from the curved attachment line near the leading edge. The grid lines in the adjacent region are also curved, eventually blending to the constant chord direction at a short distance downstream.

The side boundary solution is first generated near the root region of the wing by solving the equations with locally infinite swept-wing approximation; i.e., the local spanwise variation is neglected. However, the values of the edge velocity are used as obtained from the inviscid calculation that may have a spanwise variation. The variation of the metric coefficients in the spanwise direction is retained so that tapered wings are correctly treated. The initial upstream profile is calculated by solving the locally infinite attachment line equations.

With the $j = 1$ side boundary solution and the $i = 1$ initial profiles available, solution in the grid interior is obtained by solving the full three-dimensional equations. At each i station, solutions are obtained by sweeping in the j direction from $j = 2$ to $j = jm - 1$. The $j = jm$ point is solved using a two-point scheme for the crossflow gradient terms. At any station, the two previous i station profiles are retained for the calculation of the $\partial/\partial x$ and $\partial/\partial y$ quantities.

The wall boundary condition in the energy equation can be set for an adiabatic wall or with a prescribed heat flux or temperature distribution. For the adiabatic case δI_1 and I_1 are set to zero and H_1 is obtained as the solution. Mass injection at the wall, if any, is included while integrating the continuity equation. The solution is marched downstream until separation is indicated by a large number of iterations required for convergence.

Results

The solution procedure has been validated on several standard cases (see Table 3 of Ref. 7). Brief descriptions of three selected test cases are given here. Subsequently, results obtained for flow past a swept tapered wing and an ellipsoid at angle of attack are presented.

Supersonic Flow Past a Flat Plate

This two-dimensional test case was used to validate the generation of similarity profiles at a sharp leading edge and then calculate the two-dimensional flow downstream. The freestream conditions are $M_\infty = 3.0$, $p_\infty^* = 400$ lb/ft^2, and $T_\infty^* = 400°$R. The wall is adiabatic (from $\xi = 0$ to $\xi = 0.25$; $L^* = 1$ ft).

The similarity equations are first obtained at the leading edge by dropping the ξ gradient terms from Eqs. (11-14), resulting in

$$w' = -\frac{1}{2}F, \quad \frac{\partial}{\partial\zeta}(\bar{l}L - wF) = \frac{1}{2}F^2, \quad \frac{\partial}{\partial\zeta}(\bar{l}_3 I - wH) = \frac{1}{2}FH \tag{31}$$

The solution of the flow downstream is obtained by solving the two-dimensional version of Eqs. (11-14). Figure 3 shows the profiles of F, F', T/T_e, and H at $\xi = 0.25$ for 21 points distributed equally with $\zeta_e = 8$. The scheme, when reduced to second-order accuracy ($c_3 = c_4 = 0$), required about 70 points to achieve similar accuracy.

The method reproduced correctly the Blasius value of $C_{f-\infty}\sqrt{Re_x} = 0.664$ when run for a low Mach number value. The corresponding value for $M_\infty = 3$ is 0.6089 that compares well with the value obtained from Ref. 8.

The order of accuracy of the method was verified by varying the step size. Figure 4 shows the variation of the accuracy of solution profile as a function of $\Delta\zeta$. The error (defined as the absolute difference between the solution and the "exact" solution with $km = 161$, $\Delta\zeta = 0.05$) showed a fourth-order rate decrease. In some later applications, the ζ grid was exponentially stretched so as to cluster more points near the wall. Since the present method is a two-point scheme, the solution remains fourth-order accurate for nonuniform grids as well.

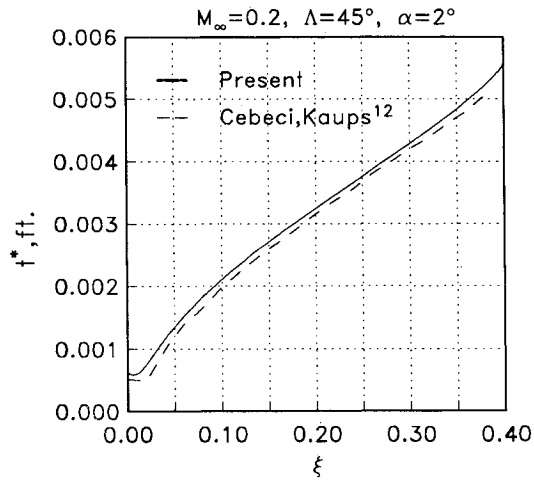

Fig. 5 Boundary-layer thickness variation on infinite swept wing.

Flow Past an Infinite Swept Wing

The infinite swept-wing equations are solved in this case; the major assumption is that the flow is independent of the spanwise coordinate. Since $\partial/\partial\eta$ terms drop out, simpler equations can be written for the attachment line and the flow downstream.

The solution at the attachment line is dependent only on the freestream Mach number and the sweep angle Λ. The numerical results (C_f, shape factor, Re_θ) agree very well with experimental data obtained by Adam.[9] For the flow downstream, the two-dimensional potential code GRUMFOIL[10] was used to calculate the external flow. The boundary-layer edge flow quantities were calculated from these results by application of the classical sweep theory[11] as follows:

$$u_e = \frac{u_{2D}\cos\Lambda}{(\cos^2\alpha_c\cos^2\Lambda + \sin^2\alpha_c)^{1/2}}, \quad v_e = \sin\Lambda\,(1 - \cos\alpha_c u_e) \tag{32}$$

where u_{2D} is the total velocity past the airfoil section normal to the leading edge. The metric quantities for this case can also be calculated as a function of α_c, Λ, and S_1, with ξ being measured along S_1 and L^* equal to the streamwise chord length.

Most of the experimental boundary-layer data on wings are for turbulent flow, and hence code validation had to be done by comparison with other numerical results. Calculations were done for a wing with a NACA 0012 cross section (streamwise) and $\Lambda = 45$ deg at $M_\infty = 0.2$ and $\alpha = 2$ deg. The results were compared with those obtained using the Cebeci, Kaups[12] code for infinite swept wings. Figure 5 shows a comparison of the

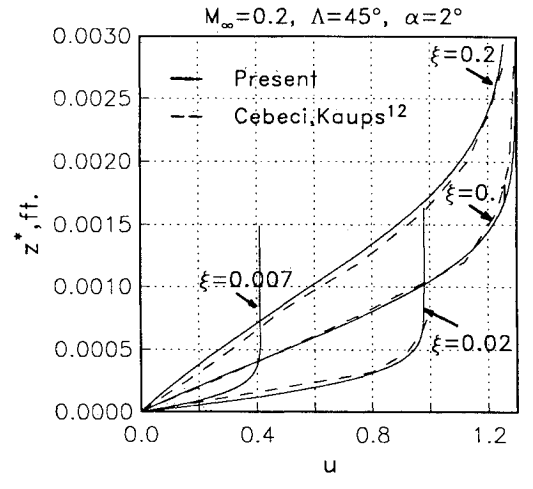

Fig. 6 Comparison of velocity profiles for infinite swept-wing flow.

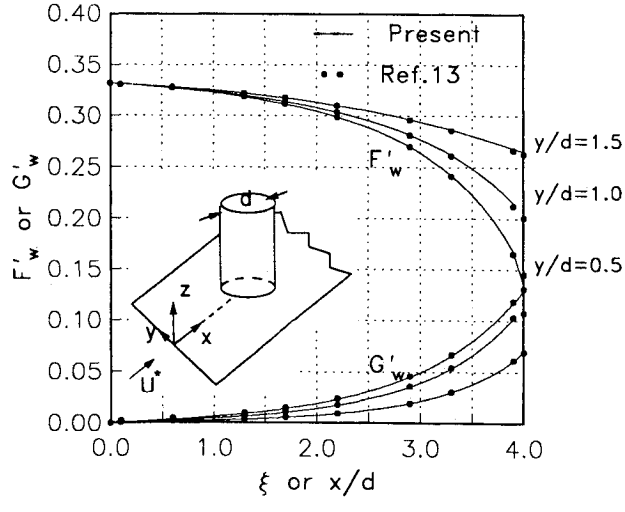

Fig. 7 Variation of F_w' and G_w' for cylinder on flat plate flow.

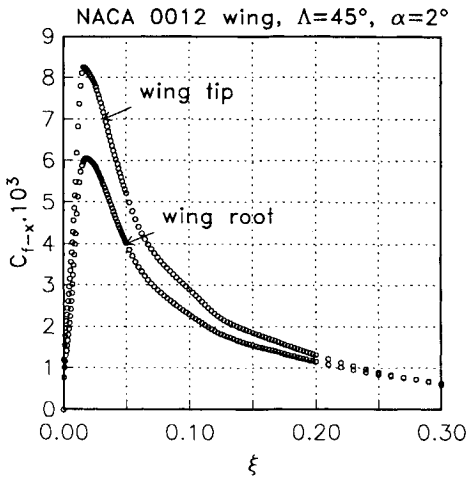

Fig. 8 Skin friction coefficient variation for swept-wing flow, upper surface.

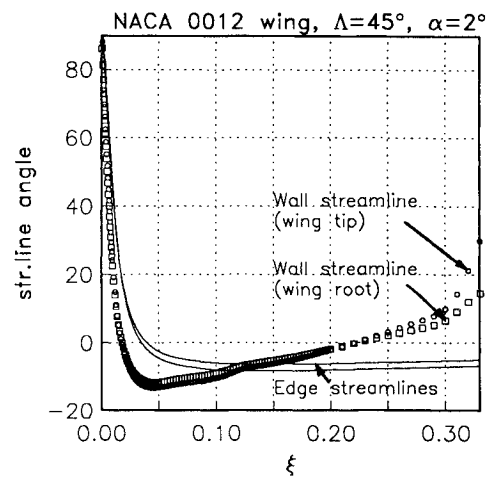

Fig. 10 Streamline angle at boundary-layer edge and at the wall, swept-wing flow, upper surface.

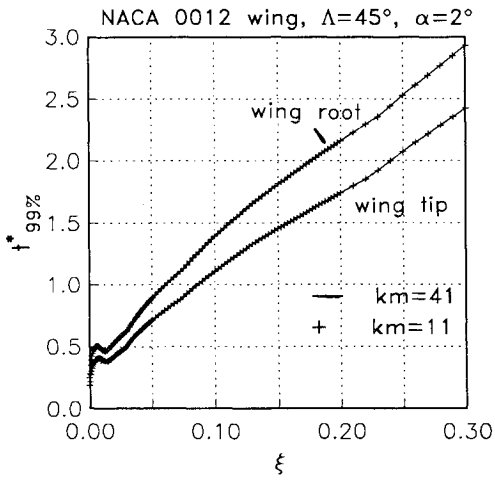

Fig. 9 Boundary-layer thickness variation for swept-wing flow, upper surface.

boundary-layer thickness variation, and Fig. 6 shows comparisons of streamwise velocity profiles at a few streamwise stations on the upper surface. Separation locations on lower and upper surfaces also agreed well between the two calculations.

Flow Around a Cylinder on a Flat Plate

This is a standard test case for three-dimensional incompressible boundary-layer flow. The flow configuration consists of a cylinder placed normal to a flat plate. The flat plate boundary layer is thus subjected to an adverse pressure gradient caused by the cylindrical obstruction, leading to flow separation. The flow is fully three-dimensional; simplifications exist in the metric coefficients due to the Cartesian grid and the inviscid flow can be obtained exactly from potential solution. The details of this test case are given by Fillo and Burbank.[13] They also present tables for F'_w and G'_w at several crossflow planes. The initial solution upstream of the cylinder is assumed to be the self-similar flat plate profile. The symmetry plane solution is generated first by solving the symmetry line equations. The full three-dimensional equations are solved subsequently. Figure 7 shows a comparison of the values of F' at the wall with results given by Fillo and Burbank (a factor of $\sqrt{2}$ is included due to different definitions). Comparison with G' values at the wall at several crossflow planes also shows very good agreement.

Calculations on a Swept Tapered Wing

An important concern in the calculation of boundary layer on wings is the generation of starting planes. If wing-alone geometry is being considered, there is a flow symmetry line at the wing root. However, at the symmetry line, the grid lines must be orthogonal. For highly swept wings, this means that constant-chord lines have to have a large curvature near the symmetry line with a large number of stations clustered in this area to resolve the geometry. In any case, a symmetric wing is an idealized case, since a real wing is attached to a fuselage and has a complex flowfield due to the interaction with the fuselage boundary layer. Consequently, in the present work, it was decided to adopt a locally infinite swept-wing assumption at a span station slightly outboard from the wing root. In this concept, the η direction variation of metrics is included so that swept tapered wings are correctly treated. The flow gradients in the η direction in the wing root plane are neglected, although the edge velocities used are those obtained from the inviscid code and, in general, have a spanwise variation.

The boundary-layer edge data are obtained from an inviscid interface, with the inviscid data generated by a potential panel code. The results presented here are for a NACA 0012 cross-section wing with $\Lambda = 45$ deg, $\alpha = 2$ deg, and a taper and aspect ratio of 0.5 and 3.0, respectively, for $M_\infty = 0.3$. The solution was obtained for both the upper and lower surfaces. Separation as seen by numerical divergence is located at 62% on the lower surface and 34% on the upper surface.

Calculations were made with 11 and 41 points in the ζ direction. The velocity profiles were predicted accurately with 11 points, which demonstrates the advantages due to the higher order of accuracy and the transformation that correctly scales the laminar boundary-layer growth. Figure 8 shows the streamwise skin friction variation at two span stations near the wing root and tip. Figure 9 shows the boundary-layer thickness variation for the same stations for $km = 11$ compared with the solution from a $km = 41$ run. The streamline angle variations at the edge of the boundary layer and the limiting values at the wall are given in Fig. 10.

Calculations on an Ellipsoid

The flow over an ellipsoid body at an angle of attack is a standard test case for a three-dimensional boundary-layer cal-

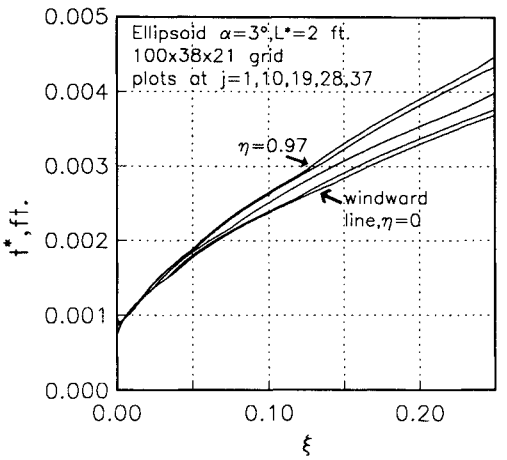

Fig. 11 Boundary-layer thickness variation on ellipsoid at $\alpha = 3$ deg.

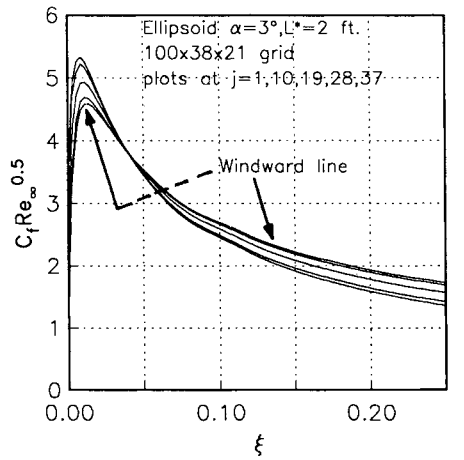

Fig. 12 Variation of skin friction coefficient on ellipsoid at $\alpha = 3$ deg.

culation. The geometry is analytic and for low-speed flow, the inviscid conditions can be obtained by an analytic formulation. However, in the present calculation, the body definition, metrics, and inviscid conditions were numerically input. In this way, the program is applicable for general bodies also, since no assumption is made about the analytic nature of the body. The inviscid conditions corresponding to a 1:4 eccentricity ellipsoid at $\alpha = 3$ deg were calculated using the Hess potential panel code.[14] The boundary-layer edge velocities were obtained from the surface Euler equations. Boundary-layer calculations were obtained for the first 25% of the body for $Re_\infty = 1.4 \times 10^5$. Figures 11 and 12 show the variation of the boundary-layer thickness and the streamwise skin friction coefficient $C_{f,x}\sqrt{Re_\infty}$ for several span locations. The present results compare well with calculations reported by Wang.[15]

Conclusions

A fourth-order accurate finite-difference scheme for solving the three-dimensional boundary-layer equations for general aerodynamic bodies has been presented. The method uses the second-order accurate zig-zag scheme in the crossflow direction. The procedure has been validated for a number of standard flow cases and has been applied to wing and ellipsoid flows. The interface between the inviscid flow and the boundary layer through solution of the surface Euler equations has been demonstrated.

The fourth-order accurate method yields accurate results for laminar flow on wings with as few as 11 points in the boundary layer. Smooth and accurate profiles required for stability analysis can be efficiently generated using the present procedure.

Appendix: Coefficients in the Transformed Three-Dimensional Boundary-Layer Equations

Coefficients for the continuity equation [Eq. (11)]

$$\tilde{A}_1 = \frac{-S_1}{h_1}, \quad \tilde{A}_2 = \frac{-S_1}{C_{13}\phi}\frac{\partial}{\partial\xi}\left(C_{13}\frac{\phi}{h_1}\right)$$

$$\tilde{A}_3 = \frac{-S_1}{h_2 u_e}, \quad \tilde{A}_4 = \frac{-S_1}{C_{13}\phi}\frac{\partial}{\partial\eta}\left(C_{13}\frac{\phi}{h_2 u_e}\right) \tag{A1}$$

Coefficients for the x momentum equation [Eq. (12)]

$$B_1 = -\tilde{A}_1, \quad B_2 = -\tilde{A}_3$$

$$B_3 = \frac{S_1}{h_1 u_e}\frac{\partial u_e}{\partial\xi} - \tilde{A}_2 + C_{24}S_1$$

$$B_4 = \frac{S_1}{h_1 u_e^2}\frac{\partial u_e}{\partial\eta} - \tilde{A}_4 + C_{25}\frac{S_1}{u_e}$$

$$B_5 = C_{26}\frac{S_1}{u_e^2}, \quad B_6 = -(\tilde{B}_3 + \tilde{B}_4 v_e + \tilde{B}_5 v_e^2)$$

$$\tilde{B}_3 = B_3 + \tilde{A}_2, \quad \tilde{B}_4 = B_4 + \tilde{A}_4 \tag{A2}$$

Coefficients for the y momentum equation [Eq. (13)]

$$C_1 = -\tilde{A}_1, \quad C_2 = -\tilde{A}_3$$

$$C_3 = C_{34}S_1 u_e$$

$$C_4 = -\tilde{A}_2 + S_1 C_{35}, \quad C_5 = -\tilde{A}_4 + C_{36}\frac{S_1}{u_e}$$

$$C_6 = -\left(C_1\frac{\partial v_e}{\partial\xi} + C_2 v_e\frac{\partial v_e}{\partial\eta} + C_3 + \tilde{C}_4 + \tilde{C}_5 v_e^2\right)$$

$$\tilde{C}_4 = C_4 + \tilde{A}_2, \quad \tilde{C}_5 = C_5 + \tilde{A}_4 \tag{A3}$$

Coefficients for the energy equation [Eq. (14)]

$$D_1 = -\tilde{A}_1, \quad D_2 = -\tilde{A}_3$$

$$D_3 = -\tilde{A}_2, \quad D_4 = -\tilde{A}_4$$

$$D_5 = \frac{u_{\infty,*}^2}{H_{\text{ref},*}}\frac{u_e^2}{2}\frac{\partial}{\partial\zeta}\left(\bar{l}\frac{1-\sigma}{\sigma}\frac{\partial}{\partial\zeta}q^2\right) \tag{A4}$$

Acknowledgment

The first author gratefully acknowledges research support received from the Computational Methods Branch, Fluid Mechanics Division of NASA Langley Research Center under Contract NAS1-17919.

References

[1]Harris, J. E., and Blanchard, D. K., "Computer Program for Solving Laminar, Transitional, or Turbulent Compressible Boundary-Layer Equations for Two-Dimensional and Axisymmetric Flow," NASA TM 83207, 1982.

[2]Bushnell, D. M., Cary, A. M., Jr., and Harris, J. E., "Calculation Methods for Compressible Turbulent Boundary Layers—1976," NASA SP-422, 1977.

[3]Wang, K. C., "On the Determination of the Zones of Influence and Dependence for Three-Dimensional Boundary-Layer Equations," *Journal of Fluid Mechanics,* Vol. 48, part 2, 1971, pp. 397–404.

[4]Hirchel, E. H., and Kordulla, W., "Shear Flow in Surface Oriented Coordinates," *Notes on Numerical Fluid Mechanics,* Vieweg, Braunschweig, Federal Republic of Germany, 1981.

[5]Anderson, O. L., "Calculation of Three-Dimensional Boundary Layers on Rotating Turbine Blades," Proceedings of the American Society of Mechanical Engineers Winter Annual Meeting, Nov. 1985, pp. 121–132.

[6]Iyer, V., and Harris, J. E., "Solution of the Surface Euler Equations for Accurate Three-Dimensional Boundary Layer Analysis of Aerodynamic Configurations," AIAA Paper 87-1154-CP, June 1987.

[7]Iyer, V., and Harris, J. E., "Three-Dimensional Compressible Boundary Layer Calculations to Fourth Order Accuracy on Wings and Fuselages," AIAA Paper 89-0130, Jan. 1989.

[8]Schlichting, H., *Boundary Layer Theory,* 7th ed., McGraw-Hill, New York, 1979, p. 337.

[9]Adams, J. C., Jr., "Numerical Calculation of the Subsonic and Transonic Turbulent Boundary Layer on an Infinite Yawed Airfoil," Arnold Engineering Development Center, Tullahoma, TN, AEDC-TR-73-112, July 1973.

[10]Mead, H. R., and Melnik, R. E., "GRUMFOIL: A Computer Code for the Viscous Transonic Flow Over Airfoils," NASA CR-3806, Oct. 1985.

[11]Shapiro, A. H., *The Dynamics and Thermodynamics of Compressible Fluid Flow,* Vol. 1, Ronald Press, New York, 1953.

[12]Kaups, K., and Cebeci, T., "Compressible Laminar Boundary Layers with Suction on Swept and Tapered Wings," *Journal of Aircraft,* Vol. 14, No. 7, July 1977, pp. 661–667.

[13]Fillo, J. A., and Burbank, R., "Calculation of Three-Dimensional Laminar Boundary Layer Flows," *AIAA Journal,* Vol. 10, No. 3, 1972, pp. 353–355.

[14]Hess, J. L., "Calculation of Potential Flow About Arbitrary Three-Dimensional Lifting Bodies," McDonnell Douglas Corporation, Rept. J5679-01, 1972.

[15]Wang, K. C., "Three-Dimensional Boundary Layer Near the Plane of Symmetry of a Spheroid at Incidence," *Journal of Fluid Mechanics,* Vol. 43, Part 1, 1970, pp. 187–209.